Radiation Heat Transfer Down an Elongated Spheroidal Cavity

Sean P. Fitzgerald and William Strieder
Dept. of Chemical Engineering, University of Notre Dame, Notre Dame, IN 46556

Effects of elongation on the radiation heat transport down a spheroidal cavity, located in a conducting solid with a diffusely reflecting cavity–solid interface, are examined. An effective conductivity λ_e and a void radiation conductivity λ_r are obtained as a function of cavity eccentricity α and surface emissivity ϵ. To facilitate the calculations and produce readily applicable equations, a rigorous variational principle is used. Exact solutions are generated in the neighborhood of the spherical cavity ($\alpha^2 \to 0$) for any $\epsilon > 0$, a long needle-shaped void ($\alpha^2 \to 1$) for any $\epsilon > 0$, and a perfect reflector ($\epsilon \to 0$) for arbitrary elongation ($0 \le \alpha^2 \le 1$). Significant differences arising from the shape change are observed. The $\alpha^2 \to 0$ edge demonstrates a linear increase in λ_r with ϵ. At the opposite edge $\alpha^2 \to 1$ and positive ϵ, λ_r is a horizontal line independent of ϵ, much like the long cylinder, whose conductivity is a factor of $32/(9\pi)$ ($= 1.13$) larger. In the neighborhood of $\epsilon \to 0$, λ_r is always zero for any $0 \le \alpha^2 \le 1$. The emissivity slope for $\epsilon \to 0$ starts from unity at $\alpha^2 = 0$ and increases monotonically with elongation to a singularity $3\pi[16(1-\alpha^2)]^{-1}$ as $\alpha^2 \to 1$ for the long needle.

Introduction

Thermal radiation across closed cavities is a contributing heat-transfer mechanism in a number of thermal engineering applications of porous materials. The cavity locations, size distribution, and shapes play a significant role in radiant energy transfer. Examples are heat transport down along straw-shaped voids in insulating firebrick (Ganguley and Hasselman, 1976), radiation heat transfer within cavities created by radiation damage of ceramic nuclear-fuel elements (Marino, 1969, 1971), void heat transfer during the high-temperature synthesis of advanced ceramics (Varma et al., 1990), and heat transfer within reduced-pressure cellular-type, cryogenic insulating materials, such as expanded pearlite or ebonite (Kaganer, 1969).

In cases where the pore microstructural lengths are small compared to the overall dimensions of the porous material, and the local temperature drop ΔT across the material is small compared to the local average temperature $\overline{T}$, a porous material effective conductivity λ_e can be rigorously formulated (Whitaker, 1980). In turn from λ_e, one can obtain a suitably *averaged local void radiation conductivity* λ_r. For example, at the point on a plot of λ_e for an evacuated porous medium, vs. the solid conductivity λ_s, that the effective conductivity curve crosses the 45° line, $\lambda_e = \lambda_s = \lambda_r$. In practice, for packed beds (Argo and Smith, 1953; Beek, 1962; Smith, 1970), insulation and the other void–solid systems just mentioned, the engineering property needed for thermal calculations is λ_e. The λ_e values are usually estimated from the solid conductivity λ_s, and a model void radiation conductivity λ_r. Other transport mechanisms can also be included in λ_e (Argo and Smith, 1953; Smith, 1970) and are normally represented by diffusive-type coefficients, for example, the heat-transfer convection coefficient. In the exact formulation of the problem, the surrounding solid is a Fourier thermal conductor, but radiation inside the voids is governed by the interfacial flux boundary condition and a nonlocal surface-to-surface integral equation with a differential view factor. In this situation, the void radiation conductivity is a useful engineering approximation, particularly when simultaneous chemical reactions (Smith, 1970, 1981), phase transformations such as evaporation (Whitaker, 1984), or void geometry changes (Sortirchos and Tomadakis, 1990) are occurring, and detailed microlevel solutions become prohibitively difficult.

Then a suitable formulation of the problem of determining λ_r would be to select the λ_r form that gives a "best" value for a rigorously defined λ_e. One fruitful approach is to use a

Correspondence concerning this article should be addressed to W. Strieder.

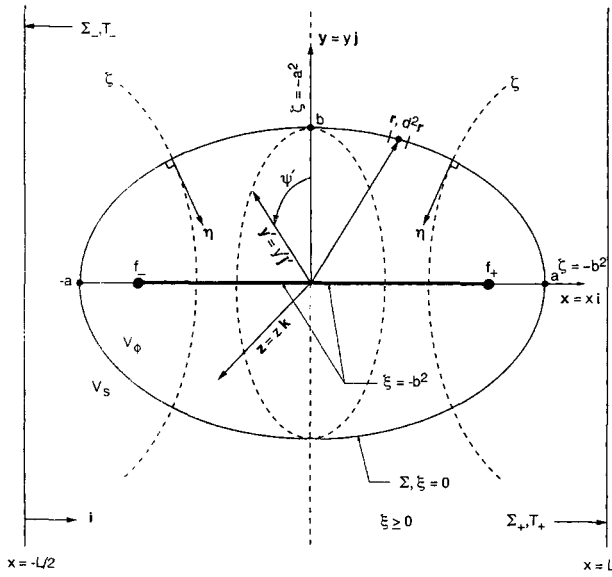

Figure 1. Prolate spheroidal cavity of major axis *a* and minor axis *b* in a solid slab.

Ellipsoidal ξ, ζ, ψ, Cartesian x, y, z, and rotated Cartesian coordinates y' are shown.

variational principle, whose global extremum value is the engineering property of interest, λ_e. By its nature, the variational principle is already written in terms of suitable volume and surface averages. Further, a careful choice of trial functions will provide at least a true bound and many times a good estimate of the extremum properties, λ_e and λ_r. As the engineering model equation for λ_e is based on a local average void radiation conductivity λ_r and a solid conductivity λ_s, operating within the specified solid–void geometry of the media (Torquato, 1987), an approximate trial function for the temperature would be the analytical solution of this corresponding two-phase Fourier heat-transfer problem (Landau et al., 1984). The trial radiosity then can be generated directly by inserting the trial temperature into the interfacial flux condition (Chiew and Glandt, 1983) that relates the radiosity, the surface temperature, and the normal temperature derivative at the void–solid interface. Identification of the λ_r can be done either from comparing the optimized trial temperature to the two-phase Fourier, exact-solution form, or by backing λ_r out of the variational expression for λ_e.

For those complex engineering systems, where heat transport is coupled to mass transfer, chemical reactions, and internal structure changes, analytical forms for λ_e and λ_r will be much less computationally demanding to use. The physical problem considered in this article is steady-state heat transfer down the axis of symmetry of a prolate spherical cavity. The advantage of the geometry is its generality: the prolate spheroid (Figure 1), with major axis a, minor axis b, and eccentricity $\alpha = \sqrt{1 - b^2/a^2}$, generates a spheroidal void in the zero eccentricity limit ($\alpha \to 0$) and a long "needle" in the opposite limit ($\alpha \to 1$). Cavity surfaces are opaque, gray, diffusely reflecting, and emitting. The resulting variational expression λ_r^* [see Eqs. 37–44 and 51] for cavity-radiation heat-transfer conductivity down a prolate spheroid is analytical in both the cavity surface emissivity ϵ and the Stefan–Boltzmann conductivity factor $4\sigma\bar{T}^3 b$. In addition, λ_r^* contains α^2 and three coefficients λ_0, λ_1, λ_2 in the form of definite integrals that will depend only on the square of the eccentricity. The first of these integrals λ_0, the dimensionless, black-surface, void radiation conductivity, is analytically evaluated [see Eq. 42 for $\lambda_0(\alpha)$]. The other two integrals λ_1 and λ_2 are straightforward numerical computations, and represent fixed constants for a given shape.

The study of the void radiation conductivity down the axis of a prolate spheroid provides a picture (see Figures 3a and 3b) of the continuous transformation from a spherical cavity, where reflections and surface emissivity play a significant role, to the opposite limit of an elongated cavity, where surface emissivity is absent from the radiation void conductivity for positive ϵ:

$$\left\{ \begin{matrix} \lim \\ \alpha^2 \to 0 \end{matrix} \right\} \lambda_r^* (4\sigma \bar{T}^3 b)^{-1} = \begin{cases} \epsilon & 0 < \epsilon \le 1 \quad (1) \\ 3\pi/4 & 0 < \epsilon \le 1. \quad (2) \end{cases}$$

$$\left\{ \begin{matrix} \lim \\ \alpha^2 \to 1 \end{matrix} \right\}$$

Both conductivities vanish at zero emissivity. In the neighborhood of either geometric limit, the λ_r^* of Eqs. 1 and 2 and the conductivity expression (Eq. 51) of this article are exact solutions for any emissivity (Tsai and Strieder, 1985). They exhibit an interesting asymmetry in the conductivity increase with elongation, that is, α^2 from 0 to 1. The conductivity changes slowly at first as the elongation from the sphere limit begins, until $\alpha^2 \approx 0.8$, when a rapid increase to the maximum value (Eq. 2) at $\alpha^2 = 1$ occurs.

On the other hand, in the neighborhood of $\epsilon \to 0$ again the variational conductivities are exact solutions for any α^2. At zero emissivity, λ_r^* is always zero for an arbitrary enclosed cavity. Some interesting and potentially useful singularities are observed in the ϵ slope at lower emissivities as the cavity is elongated. Our results predict a positive slope for $\lambda_r^* (4\sigma\bar{T}^3 b)^{-1}$ with ϵ, of unit magnitude on the sphere side $\alpha^2 \to 0$, increasing with elongation to a singular value $3\pi[16(1-\alpha^2)]^{-1}$ as $\alpha^2 \to 1$. As the void cavity elongates, a knee develops in the conductivity vs. ϵ curves for fixed α^2 at a critical emissivity $\tilde{\epsilon}(\alpha^2)$. Below the critical emissivity $\tilde{\epsilon}$, the increase in conductivity with ϵ is very rapid, whereas above the knee the conductivity exhibits little change from an asymptotic value. As these curves shift to higher elongation $\alpha^2 \to 1$, $\tilde{\epsilon}$ moves to the origin and the conductivity becomes a simple step function from 0 to Eq. 2.

In the next section of this article, the fundamental equations will be formulated. The variational principle and its relation to λ_e will be derived in the third section. The fourth section will introduce the ellipsoidal geometry and develop the trial functions referred to earlier. The fifth section will include some details of the calculations, for example, the one-dimensional kernel for surface-to-surface transport down a prolate ellipsoid, along with the results. The final section will discuss the results and end with the summary and conclusions.

Fundamental Equations

The system (Figure 1) is a large solid slab of total volume V made up of two regions. The first is a prolate spheroidal void section of volume V_ϕ at the slab's center. The prolate

spheroid's axis of symmetry lies along the unit vector i pointing in the x direction across the slab's length. The other region is a solid of volume V_s and thermal conductivity λ_s. The solid has three surfaces—a plane surface Σ_- perpendicular to i at $x = -L/2$, a plane surface Σ_+ perpendicular to i at $x = L/2$, and an interfacial surface Σ between the regions V_s and V_ϕ.

The emitted radiative flux from a surface element d^2r at r on Σ is dependent upon the surface emissivity ϵ, the Stefan–Boltzmann constant σ, and the absolute temperature $T(r)$ to the fourth power, $\epsilon\sigma T^4(r)d^2r$. The radiation arriving at a unit element of surface located at r on Σ follows Kirchoff's law, absorbing a fraction ϵ of the incident radiation, and diffusely reflecting the fraction $1-\epsilon$. Defining the radiant flux incident on a unit surface at r as the function $H(r)$, the total radiation diffusely leaving a unit surface at r, that is, the radiosity $B(r)$, is

$$B(r) = \epsilon\sigma T^4(r) + (1-\epsilon)H(r) \qquad (r \text{ on } \Sigma). \tag{3}$$

To calculate the radiant energy transfer between different elements of the prolate spheroidal cavity it is necessary to define the differential view factor. $K(r',r)d^2r$ is the fraction of radiation, diffusely distributed, leaving a unit surface element located at r', that travels a straight-line free path and arrives at a second surface element d^2r located at r on Σ. $K(r',r)d^2r$ is used to formulate the radiant exchange between surfaces. The assumption of diffuse emission and scattering from the surface of Σ gives the K form of Lambert's cosine law (Siegel and Howell, 1992):

$$K(r',r) = K(r,r'), \tag{4}$$

and

$$K(r',r) = -\frac{[\eta(r)\cdot\rho][\eta(r')\cdot\rho]}{\pi\rho^4}. \tag{5}$$

The vectors $\eta(r)$ and $\eta(r')$ in Eq. 5 are the unit normals pointing into the void at the points r and r', respectively, on the surface Σ. The vector ρ points from r to r', with ρ as its magnitude. The factor $K(r',r)d^2r$ is a probability, so its sum over the surface Σ is unity

$$\int_\Sigma d^2r' K(r,r') = 1. \tag{6}$$

Of the radiation leaving the surface element d^2r' at r' on Σ, $B(r')d^2r'$, only the fraction $B(r')d^2r'K(r',r)$ will travel directly to the unit surface element at r on Σ. The sum of these differential incident fluxes over Σ gives the total flux onto the unit surface element at r

$$\int_\Sigma K(r',r)B(r')d^2r' = H(r) \qquad (r \text{ on } \Sigma). \tag{7}$$

Substituting $H(r)$ from Eq. 3 into Eq. 7 and subtracting the radiosity at the point r on the surface from both sides of Eq. 7, creates an integral equation in terms of the temperature and radiosity

$$\int_\Sigma K(r',r)[B(r') - B(r)]d^2r' = \frac{\epsilon}{1-\epsilon}[B(r) - \sigma T^4(r)] \qquad (r \text{ on } \Sigma), \tag{8}$$

where the unity integral property (Eq. 6) was used to obtain Eq. 8.

The combination of the steady-state energy balance and Fourier's law for a point r within the solid V_s provides

$$\nabla\cdot[\lambda_s\nabla T(r)] = 0 \qquad (r \text{ in } V_s). \tag{9}$$

The thermal boundary condition equating the net radiative flux from the void–solid surface Σ at r to the normal Fourier flux from the solid is

$$-\lambda_s\eta\cdot\nabla T(r) = B(r) - H(r) \qquad (r \text{ on } \Sigma). \tag{10}$$

Further, the substitution of Eq. 3 into Eq. 10 eliminates H in favor of B and T,

$$\lambda_s\eta\cdot\nabla T(r) = \frac{\epsilon}{1-\epsilon}[B(r) - \sigma T^4(r)] \qquad (r \text{ on } \Sigma). \tag{11}$$

The equations of the total incident flux (Eq. 8), Fourier's law in the solid, and the thermal boundary condition (Eq. 11) at the void–solid surface Σ, when coupled with the temperature end conditions of the slab,

$$T(r) = \begin{cases} T_- & (r \text{ on } \Sigma_-) \quad (12a) \\ T_+ & (r \text{ on } \Sigma_+), \quad (12b) \end{cases}$$

are in principle enough to determine the radiosity and temperature. This knowledge will in turn yield the net flux across the composite slab (Figure 1) and the effective conductivity λ_e.

The fundamental equations just given need their temperature dependencies linearized to calculate the effective conductivity and the radiation conductivity. The average slab temperature $\bar{T}$ is defined using the steady-state end surface temperatures T_- and T_+

$$\bar{T} = \frac{T_- + T_+}{2}. \tag{13}$$

The linearization assumes that the temperature difference across the slab is small compared with the average slab temperature:

$$\frac{\Delta T}{\bar{T}} = \frac{T - \bar{T}}{\bar{T}} \ll 1. \tag{14}$$

Since the radiation conductivity λ_r depends explicitly on $\bar{T}$, it is well defined only in the limit in which $\Delta T/\bar{T}$ is very small, Eq. 14. In practice this condition can be applied locally, and is appropriate here over the derivation volume. The Stefan–Boltzmann law, after neglecting terms of second order in $\Delta T/\bar{T}$, and including terms zeroth and first order, has the form

$$I(r) = \sigma T^4(r) = A + CT(r), \tag{15a}$$

where

$$A = -3\sigma \bar{T}^4, \tag{15b}$$

and

$$C = 4\sigma \bar{T}^3. \tag{15c}$$

One result of the small temperature gradient is the opportunity to also rigorously neglect the temperature dependence in the solid conductivity and surface emissivity and evaluate both at $\bar{T}$. Equations 8, 9, and 11 with the substitution of Eqs. 15a, 15b, and 15c, and the coefficients ϵ and λ_s evaluated in $\bar{T}$, are now linear in the temperature and radiosity.

Variational Principle for λ_e

A variational upper bound on the net heat flux Q, averaged perpendicularly to the x-axis over any cross section of the slab (Figure 1), will be derived in this section for an arbitrary cavity geometry. For steady state, the net average heat flux Q across the planar surfaces Σ_- or Σ_+, located at $x = -L/2$ and $x = L/2$, with respective uniform temperatures T_- and T_+, is the same. The dot product of Q with β can be written in terms of a surface integration over Σ_- and Σ_+ as

$$-Q\cdot\beta = \frac{1}{V}\int_{\Sigma_- + \Sigma_+} d^2r CT(r)\,\lambda_s \eta\cdot\nabla T(r), \tag{16}$$

where η points away from the solid and

$$\beta = C(T_+ - T_-)L^{-1}i = C\theta i = C\theta. \tag{17}$$

The upper bound on the heat flux comes from the variational functional

$$V\Gamma\{B^*, I^*\} = \int_{V_s} d^3r \lambda_s [\nabla I^*(r)]^2 + \frac{\epsilon}{1-\epsilon} C\int_\Sigma d^2r [B^*(r) - I^*(r)]^2 + \frac{1}{2}C\int_\Sigma d^2r \int_\Sigma d^2r' K(r,r')[B^*(r) - B^*(r')]^2. \tag{18}$$

For convenience a trial function,

$$I^*(r) = A + CT^*(r), \tag{19a}$$

based on the linearized form of the black-body emission flux (Eq. 15) with the constants A and C, has been introduced in place of the trial temperature T^*. As with the trial temperature, I^* must be continuous, as well as piecewise continuously differentiable in V_s, and satisfy the thermal end boundary conditions

$$I^*(r) = \begin{cases} I_- = A + CT_- & (r \text{ on } \Sigma_-) \quad (19b) \\ I_+ = A + CT_+ & (r \text{ on } \Sigma_+). \quad (19c) \end{cases}$$

To derive the variational upper bound, trial functions for the surface radiosity B^* and the thermal trial function I^*, written in the form of the corresponding exact solutions (B and $I = A + CT$) of the transport equations of the preceding section, in addition to their variations (δB and $\delta I = C\delta T$), are generated,

$$B^* = B + \delta B \tag{20a}$$

and

$$I^* = I + \delta I. \tag{20b}$$

A substitution of Eqs. 20a and 20b into the variational integrals (Eq. 18) of Γ will generate three parts, a zeroth-order term $\Gamma\{B, I\}$ in the variation, a term $\delta\Gamma$ containing all integrand products first order in the variation, and, for this simple quadratic form (Eq. 18) a second-order term $\delta^2\Gamma$ in the variation.

$$\Gamma\{B^*, I^*\} = \Gamma\{B, I\} + \delta\Gamma + \delta^2\Gamma. \tag{21}$$

As the surface to surface jump probability K given in Eq. 5, the constant C from Eq. 15c, and the interfacial resistance factor $\epsilon(1-\epsilon)^{-1}$ are always positive, the second-order terms of the quadratic $\delta^2\Gamma$ must be positive for any trial function and zero for the exact solution

$$\delta^2\Gamma \geq 0. \tag{22}$$

All first-order terms in the variation ($\delta B, \delta I$) from Eq. 18 are now collected in $\delta\Gamma$. The first integral in the righthand side is integrated by parts, and the divergence theorem is applied over V_s. In the last integral the variables r and r' are interchanged and the K symmetry condition (Eq. 4) is applied, to obtain

$$\begin{aligned} \frac{1}{2}V\delta\Gamma = &\int_{\Sigma_- + \Sigma_+} d^2r \delta I(r)\eta\cdot[\lambda_s\nabla I(r)] \\ &- \int_{V_s} d^3r \delta I(r)\nabla\cdot[\lambda_s\nabla I(r)] \\ &+ \int_\Sigma d^2r \delta I(r)\eta\cdot[\lambda_s\nabla I(r)] \\ &- \frac{\epsilon}{1-\epsilon}C\int_\Sigma d^2r\,\delta I(r)[B(r) - I(r)] \\ &+ \frac{\epsilon}{1-\epsilon}C\int_\Sigma d^2r\,\delta B(r)[B(r) - I(r)] \\ &- C\int_\Sigma d^2r\,\delta B(r)\int_\Sigma d^2r' K(r,r')[B(r') - B(r)]. \end{aligned} \tag{23}$$

To show that this form vanishes we note:

1. The first integral in Eq. 23 is zero because the boundary conditions, Eqs. 19b and 19c, require $\delta I = 0$ on Σ_- and Σ_+.

2. The second integral vanishes due to the solid phase, differential energy balance (Eq. 9), written in terms of I from Eq. 15.

3. The third and fourth integrals, which depend on δI, combine to form the interfacial condition, Eq. 11, with I again given by Eq. 15, and cancel.

4. The fifth and sixth integrals in Eq. 23, first order in the variation δB, together vanish from the surface energy balance, Eq. 8; and hence

$$\delta\Gamma = 0. \tag{24}$$

Then from Eqs. 21, 22, and 24, the variational integrals (Eq. 18) are indeed a rigorous upper bound principle on the zeroth-order term

$$\Gamma\{B, I\} \leq \Gamma\{B^*, I^*\}. \tag{25}$$

To relate $\Gamma\{B, I\}$ to the heat flux, one can start again with the variational integrals (Eq. 18), but now written in terms of the true B and I, and repeat exactly the same steps used to derive Eq. 23. The resulting $\Gamma\{B, I\}$ is the same form as Eq. 23 for $V\delta\Gamma/2$, but with the variations $(\delta B, \delta I)$ replaced by the true solutions (B, I) on the righthand side. As is the steps 2, 3, and 4, all terms will vanish except the first integral, which is now written using Eq. 15a for I in terms of T

$$V\Gamma\{B, A + CT\} = \int_{\Sigma_- + \Sigma_+} d^2\boldsymbol{r}[A + CT(\boldsymbol{r})]C\lambda_s\boldsymbol{\eta}\cdot\nabla T(\boldsymbol{r}). \tag{26}$$

The $\boldsymbol{\eta}$ points outward away from the slab, in the $\boldsymbol{i}$ direction on Σ_+ and negative $\boldsymbol{i}$ direction on Σ_-. For steady-state heat transfer across the slab the A integral vanishes because the net heat-transfer flux $\boldsymbol{Q}$ is constant across the slab. From Eq. 16

$$\Gamma\{B, A + CT\} = -C\boldsymbol{Q}\cdot\boldsymbol{\beta} = C^2\theta^2\lambda_e, \tag{27}$$

where the effective thermal conductivity of the slab (Figure 1) is λ_e $(= |Q/\theta|)$. Then from inequality 25 and Eqs. 19a and 26, the rigorous variational upper bound on λ_e is

$$\lambda_e \leq C^{-2}\theta^{-2}\Gamma\{B^*, A + CT^*\}. \tag{28}$$

If the exact solutions B and T are substituted into the variational integrals Γ of Eqs. 18, 19, and 28, the true value of λ_e is obtained, otherwise the result is an upper bound on λ_e.

Ellipsoidal Geometry and Trial Functions

Following the procedure discussed in the Introduction, and using the conductivities λ_s in the solid and an unspecified parameter as the void conductivity value $\bar{\lambda}_r$, the temperature trial function is generated by solving the equivalent two-phase conduction problem. Then the radiosity trial function is obtained by plugging the trial temperature into the interfacial equation, Eq. 11. The variational principle permits the selection of a λ_r^* that directly optimizes the calculated value of λ_e. The cavity geometry of interest is the volume of revolution generated by rotating an ellipse

$$\frac{x^2}{a^2 + u} + \frac{y^2}{b^2 + u} = 1, \tag{29}$$

for the case $u = 0$ about its major axis (Figure 1). As both the solution of Eq. 9 and the normal derivative in Eq. 11 are most naturally expressed in prolate spheroidal coordinates (Landau et al., 1984), these are included in Figure 1 (ξ, ζ, ψ). The angular variable ψ runs from 0 to 2π

$$0 \leq \psi \leq 2\pi. \tag{30}$$

The elliptical coordinates ξ and ζ are the roots for u from the quadratic equation, Eq. 29, with possible values of $-b^2 \leq \xi$ and $-a^2 \leq \zeta \leq -b^2$. Confocal ellipsoids are generated for every value of ξ starting with the case $\xi = -b^2$, which runs between the two focal points f_+ and f_- as shown in Figure 1, and the value $\xi = 0$, which generates the surface of the cavity under consideration. The coordinate ζ, starting with $\zeta = -a^2$ along the y-axis specifies hyperboloids both orthogonal to and confocal with the ellipsoids, as shown in Figure 1. Hence the constant ζ lines are normal to the ellipsoidal cavity surface. The vector $\boldsymbol{r}$ is also represented in the Cartesian reference frame (x, y, z) in Figure 1.

A solution for the problem of conduction down the axis of a prolate spheroidal inclusion of conductivity $\bar{\lambda}_r$ within a long solid slab of conductivity λ_s can be found in Landau et al. (1984), and has the form

$$T^*(\boldsymbol{r}) = \bar{T} + \boldsymbol{\theta}\cdot\boldsymbol{r} + P\boldsymbol{\theta}\cdot\boldsymbol{r}[F(\xi)/F_0] \qquad (\boldsymbol{r} \text{ in } V_s). \tag{31a}$$

The vector $\boldsymbol{r}$ in Eq. 31a is taken from the center of the cavity (Figure 1),

$$F(\xi) = \int_\xi^\infty d\xi'\{\xi' + a^2\}^{-3/2}\{\xi' + b^2\}^{-1}, \tag{31b}$$

$F_0[= F(0)]$ is Eq. 31b evaluated at $\xi = 0$, and for the two-phase, $\bar{\lambda}_r$, λ_s model

$$\bar{P}(\bar{\lambda}_r) = F_0\{\lambda_s - \bar{\lambda}_r\}\{[2a^{-1}b^{-2} - F_0]\lambda_s + F_0\bar{\lambda}_r\}^{-1}, \tag{32}$$

$\bar{P}$ is a function of the variable parameter $\bar{\lambda}_r$. An optimization of the variational principle with $\bar{\lambda}_r$ in Eq. 31a or P is equivalent, but the latter is more convenient. The trial temperature T^* is then Eq. 31a and 31b, where P is treated as an optimizable parameter. Note that the trial T^* will always satisfy Laplace's equation (Eq. 9) in the solid.

To formulate a corresponding trial radiosity, the trial temperature, Eqs. 31a and 31b, is substituted into the linearized (Eq. 15a) version of the interfacial energy balance (Eq. 11). This generates the trial radiosity

$$B^*(\boldsymbol{r}) = A + C\bar{T} + \mu\{C[T^*(\boldsymbol{r}) - \bar{T}] + \omega Cb\boldsymbol{\theta}\cdot\boldsymbol{\eta}(\boldsymbol{r})\} \qquad (\boldsymbol{r} \text{ on } \Sigma). \tag{33}$$

The ω form directly generated by Eqs. 11 and 31,

$$\bar{\omega} = \mu^{-1}\frac{(1-\epsilon)}{\epsilon}\left(\frac{\lambda_s}{Cb}\right)[1 + (F_0 - 2a^{-1}b^{-2})F_0^{-1}P], \tag{34}$$

could be used in the trial radiosity (Eq. 33), but rather ω is left as a parameter to optimize λ_e. If the trial forms of T^* and B^* are the correct ones for the solution of the equations of the second section, the optimization will select Eq. 34 with P given by $\bar{P}$ of Eq. 32. The parameter μ is included in the trial radiosity (Eq. 33) to ensure the correct radiative heat-transfer conductivities for cavities with low emissivity surfaces, ($\lim_{\epsilon \to 0} \lambda_r = 0$). The optimum μ will vanish with perfect reflection ($\mu \to 0$ for $\epsilon \to 0$) to give a constant trial radiosity from Eq. 33, and approach unity for a black surface ($\mu \to 1$ for $\epsilon \to 1$) for which Eq. 33 becomes the black-body radiosity.

The trial functions, Eqs. 31 and 33, generate exact solutions for three limiting cases, $\alpha^2 \to 0$ for any ϵ, $\alpha^2 \to 1$ for any ϵ, and as discussed earlier, $\epsilon \to 0$ for any α^2. The spherical inclusion ($\alpha^2 \to 0$) solution is well known (Devera and Strieder, 1977; Tsai and Strieder, 1985). For the long-needle limit ($\alpha^2 \to 1$), the term $\boldsymbol{\theta} \cdot \boldsymbol{\eta}$ from the $\boldsymbol{\eta} \cdot \nabla T^*$ differentiation vanishes at all surface points Σ, but the ends, that is, $-a < x < a$. As a result, the radiosity (Eq. 33) approaches the black-body form linear in x on the surface, the righthand side of the integral balance, Eq. 8, vanishes, and from Appendix B the one-dimensional surface-scattering kernel reduces to that of a long cylinder, for which the linear radiosity function is a known solution. At the ends $x = \pm a$, the cavity cross section, local radius, and surface-scattering free path length all go to zero, which makes the ends of the needle perfect insulators. This sets the $\bar{\omega}$, the $\boldsymbol{\eta} \cdot \nabla T$ term in Eq. 11 and the righthand side of Eq. 8 to zero. The K integrals in Eq. 8, anchored at the ends, $\boldsymbol{r}(\pm a, 0, 0)$, vary as the free path length and hence also vanish. Equations 8–12 are satisfied and the temperature flux lines near the ends, corresponding to $\bar{\omega} = 0$, are those of an insulating inclusion.

Calculations and Results

The trial temperature function in the form of I^* from Eqs. 19a, 31a, and 31b, along with the trial radiosity (Eq. 33) for B^* are substituted into the variational integrals (Eq. 18) of Γ. Inequality 28 allows the resulting integrals to be written directly in terms of the effective conductivity, the needed transport property. At this point, it is helpful to define several averages, a volume average over the solid

$$\langle g(\boldsymbol{r}) \rangle_s = V_s^{-1} \int_{V_s} d^3 \boldsymbol{r} g(\boldsymbol{r}), \tag{35a}$$

and a cavity surface average

$$\langle g(\boldsymbol{r}, \boldsymbol{r}') \rangle_\Sigma = \Sigma^{-1} \int_\Sigma d^2 \boldsymbol{r} \int_\Sigma d^2 \boldsymbol{r}' K(\boldsymbol{r}, \boldsymbol{r}') g(\boldsymbol{r}, \boldsymbol{r}'), \tag{35b}$$

where $g(\boldsymbol{r})$ or $g(\boldsymbol{r}, \boldsymbol{r}')$ are arbitrary functions defined for $\boldsymbol{r}$ and $\boldsymbol{r}'$ on V_s or Σ. Also note, if g depends only on one surface point $\boldsymbol{r}$ in Eq. 35b, the property Eq. 6 of K allows the reduction

$$\langle g(\boldsymbol{r}) \rangle_\Sigma = \Sigma^{-1} \int_\Sigma d^2 \boldsymbol{r} g(\boldsymbol{r}). \tag{35c}$$

Expressed explicitly in terms of the variational parameters P, μ, ω, the dimensionless effective conductivity $\lambda_e (Cb)^{-1}$ becomes

$$\lambda_e (Cb)^{-1} \le \Gamma_0 + 2P\Gamma_1 + P^2 \Gamma_2 + 2\mu(1+P)^2 \Gamma_3 + 2\mu\omega(1+P)\Gamma_4 + \mu^2 (1+P)^2 \Gamma_5 + 2\mu^2 \omega (1+P)\Gamma_6 + \mu^2 \omega^2 \Gamma_7, \tag{36a}$$

where

$$\Gamma_0 = (1-\phi)\lambda_s (Cb)^{-1} + \phi\chi_0, \tag{36b}$$

$$\Gamma_1 = (1-\phi)\lambda_s (Cb)^{-1} \gamma_1 + \phi\chi_0, \tag{36c}$$

$$\Gamma_2 = (1-\phi)\lambda_s (Cb)^{-1} \gamma_2 + \phi\chi_0, \tag{36d}$$

$$\Gamma_3 = -\phi\chi_0, \tag{36e}$$

$$\Gamma_4 = -\phi\chi_1, \tag{36f}$$

$$\Gamma_5 = \phi\lambda_0 + \phi\chi_0, \tag{36g}$$

$$\Gamma_6 = \phi\lambda_1 + \phi\chi_1, \tag{36h}$$

and

$$\Gamma_7 = \phi\lambda_2 + \phi\chi_2. \tag{36i}$$

Opportunities for cancellation or simplification are likely, but only after optimum values of the variational parameters are selected.

Evaluation of the various γ, χ, and λ integrals in Eqs. 36b–36i requires integration over the ellipsoidal cavity surface and volume. These integrations are briefly discussed in Appendices A and B. The integral γ_2, which contains the function $F(\xi)$ from Eq. 31b with its value F_0 on Σ,

$$\gamma_2 = \langle [\nabla (\boldsymbol{Fi} \cdot \boldsymbol{r} F_0^{-1})]^2 \rangle_s \tag{37a}$$

is expressed in terms of the volume average (Eq. 35a). Since the trial temperature, Eqs. 31a and 31b, that has been selected, already satisfies the Laplace equation, Eq. 9, in V_s, the quantity $\nabla^2 (\boldsymbol{Fi} \cdot \boldsymbol{r} F_0^{-1})$ is zero, and after integration by parts

$$\gamma_2 = \langle \nabla \cdot [(\boldsymbol{Fi} \cdot \boldsymbol{r} F_0^{-1}) \nabla (\boldsymbol{Fi} \cdot \boldsymbol{r} F_0^{-1})] \rangle_s. \tag{37b}$$

The application of the divergence theorem over V_s with vanishing of F on Σ_- and Σ_+, transforms Eq. 37b into a surface average of the form (Eq. 35c)

$$\gamma_2 = \frac{2\phi}{m(1-\phi)} \langle \boldsymbol{i} \cdot \boldsymbol{r} \boldsymbol{\eta} \cdot \nabla (\boldsymbol{Fi} \cdot \boldsymbol{r} F_0^{-1}) \rangle_\Sigma, \tag{37c}$$

where $\phi [= (V - V_s)/V]$ is the cavity volume fraction and $m [= 2(V - V_s)/\Sigma]$ is the average pore radius. Differentiating $\boldsymbol{Fi} \cdot \boldsymbol{r} F_0^{-1}$, normal to the surface Σ in the ζ direction, we have

$$\gamma_2 = \frac{2\phi}{m(1-\phi)}\left(\frac{F_0 - 2a^{-1}b^{-2}}{F_0}\right)\langle \boldsymbol{i}\cdot\boldsymbol{r}\boldsymbol{i}\cdot\boldsymbol{\eta}\rangle_\Sigma, \quad (37d)$$

or

$$\gamma_2 = -\phi(F_0 - 2a^{-1}b^{-2})(1-\phi)^{-1}F_0^{-1}. \quad (37e)$$

In a similar fashion for the other γ volume integration,

$$\gamma_1 = \langle \boldsymbol{i}\cdot\nabla(F\boldsymbol{i}\cdot\boldsymbol{r}F_0^{-1})\rangle_s \quad (38a)$$

transforms to a surface average

$$\gamma_1 = \frac{2\phi}{m(1-\phi)}\langle \boldsymbol{i}\cdot\boldsymbol{r}\boldsymbol{i}\cdot\boldsymbol{\eta}\rangle_\Sigma, \quad (38b)$$

or

$$\gamma_1 = -\phi(1-\phi)^{-1}. \quad (38c)$$

The χ surface integrations involve three different integrands in a surface average of the type, Eq. 35c, and an emissivity factor $\epsilon(1-\epsilon)^{-1}$. These integrations are discussed briefly and performed in Appendix A. The first case

$$\chi_0 = \frac{2}{mb}\frac{\epsilon}{(1-\epsilon)}\langle(\boldsymbol{i}\cdot\boldsymbol{r})^2\rangle_\Sigma. \quad (39a)$$

Upon integration over the ellipsoidal surface Σ, using the integral, Eq. A6, and $\Lambda_{2,0}$ of Appendix A, gives

$$\chi_0 = \frac{3}{4}\frac{\epsilon}{(1-\epsilon)}\frac{1}{\sqrt{1-\alpha^2}}\left\{1 - \frac{1}{2\alpha^2} + \frac{\arcsin\alpha}{2\alpha^3\sqrt{1-\alpha^2}}\right\}. \quad (39b)$$

The second χ integral

$$\chi_1 = \frac{2}{m}\frac{\epsilon}{(1-\epsilon)}\langle \boldsymbol{i}\cdot\boldsymbol{r}\boldsymbol{i}\cdot\boldsymbol{\eta}\rangle_\Sigma \quad (40a)$$

has the same surface average as Eq. 38b. Using the integral, Eq. A7, of Appendix A, we have

$$\chi_1 = -\epsilon(1-\epsilon)^{-1}. \quad (40b)$$

The third χ surface integral

$$\chi_2 = \frac{2b}{m}\frac{\epsilon}{(1-\epsilon)}\langle(\boldsymbol{i}\cdot\boldsymbol{\eta})^2\rangle_\Sigma \quad (41a)$$

upon integration over the ellipsoid, using $\Lambda_{0,2}$ and Eq. A8 of Appendix A, becomes

$$\chi_2 = \frac{3}{2}\frac{\epsilon}{(1-\epsilon)}\frac{(1-\alpha^2)^{3/2}}{\alpha^2}\left\{-1 + \frac{\arcsin\alpha}{\alpha\sqrt{1-\alpha^2}}\right\}. \quad (41b)$$

The two-point surface integrations λ are expressed in terms of the double surface average, Eq. 35b, and explicitly contain $K(\boldsymbol{r},\boldsymbol{r}')d^2\boldsymbol{r}'$, the differential view factor. Since $\boldsymbol{i}\cdot\boldsymbol{\rho}/m$, $\boldsymbol{i}\cdot\boldsymbol{\eta}$ and $\boldsymbol{i}\cdot\boldsymbol{\eta}'$, can be expressed directly in terms of the coordinate variables (Figure 1) x and x', these integrations can be reduced to a simpler form by the introduction of the one-dimensional kernel $K(x,x')$ discussed in Appendix B. The first double surface integral

$$\lambda_0 = \langle(\boldsymbol{i}\cdot\boldsymbol{\rho})^2\rangle_\Sigma(bm)^{-1} \quad (42a)$$

written in terms of $K(x,x')[=\int_{\Sigma_{dx}}d^2\boldsymbol{r}\int_{\Sigma_{dx'}}d^2\boldsymbol{r}'K(\boldsymbol{r},\boldsymbol{r}')]$, where Σ_{dx} is just the cavity surface fraction within the one-dimensional interval dx, has the form

$$\lambda_0 = \frac{3}{8\pi ab^3}\int_{-a}^{a}dx\int_{-a}^{a}dx'\,K(x,x')(x'-x)^2. \quad (42b)$$

The one-dimensional kernel form is developed in Appendix B and its explicit form is expressed in Eq. B6. When the one-dimensional kernel function (Berman, 1965; Strieder and Prager, 1967; Verhoff and Strieder, 1971) for a prolate spheroid pore structure, Eq. B6, is substituted into Eq. 42b, this integral can be evaluated analytically:

$$\lambda_0 = \frac{3}{2}\frac{\sqrt{1-\alpha^2}}{\alpha^2}\left\{-1 + \frac{\arcsin\alpha}{\alpha\sqrt{1-\alpha^2}}\right\}. \quad (42c)$$

The second double surface integral

$$\lambda_1 = \langle[\boldsymbol{i}\cdot\boldsymbol{\rho}][\boldsymbol{i}\cdot(\boldsymbol{\eta}'-\boldsymbol{\eta})]\rangle_\Sigma m^{-1} \quad (43a)$$

with $\boldsymbol{i}\cdot\boldsymbol{\rho}$, $\boldsymbol{i}\cdot\boldsymbol{\eta}$, $\boldsymbol{i}\cdot\boldsymbol{\eta}'$, and $K(\boldsymbol{r},\boldsymbol{r}')$ in one-dimensional form becomes

$$\lambda_1 = \frac{3}{8\pi a^2 b}\int_{-a}^{a}dx\int_{-a}^{a}dx'\,K(x,x')(x'-x) \times\left[\frac{x}{\sqrt{a^2-\alpha^2x^2}} - \frac{x'}{\sqrt{a^2-\alpha^2(x')^2}}\right]. \quad (43b)$$

The third double surface integral

$$\lambda_2 = \frac{b}{m}\langle[\boldsymbol{i}\cdot(\boldsymbol{\eta}'-\boldsymbol{\eta})]^2\rangle_\Sigma, \quad (44a)$$

reduced to integration over x and x',

$$\lambda_2 = \frac{3b}{8\pi a^3}\int_{-a}^{a}dx\int_{-a}^{a}dx'\,K(x,x') \times\left[\frac{x}{\sqrt{a^2-\alpha^2x^2}} - \frac{x'}{\sqrt{a^2-\alpha^2(x')^2}}\right]^2. \quad (44b)$$

Plots of λ_0, λ_1, and λ_2 vs. the eccentricity are shown in Figure 2.

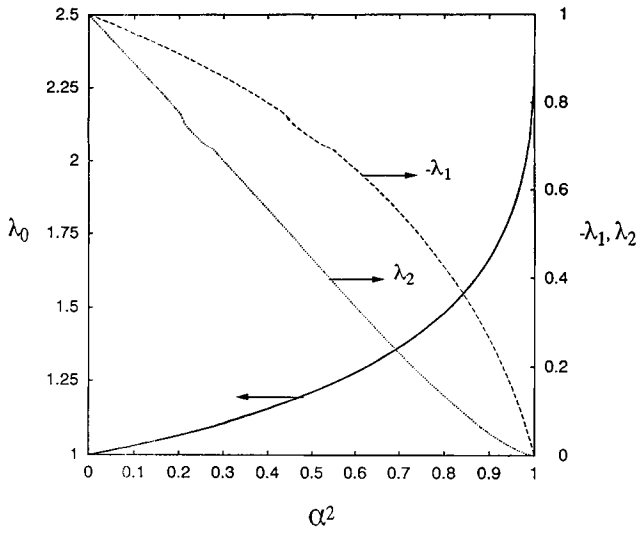

Figure 2. Values of λ_0, $-\lambda_1$, and λ_2, respectively, from Eqs. 42c, 43b, and 44b, vs. the eccentricity squared: Note that λ_1 is always negative and the corresponding positive value $(-\lambda_1)$ is shown here.

Optimum values of P and ω are obtained by minimizing the upper bound function, Eqs. 36a–36i, to obtain the "best" value of $\lambda_e(Cb)^{-1}$ for a fixed value of the parameter μ. The optimum expression for P is the same as the exact solution of the equivalent two-phase conduction problem with constant conductivities λ_s and $\bar{\lambda}_r$. The optimum is given by Eq. 32

$$P_{\text{opt}} = \bar{P}(\lambda_r^*), \tag{45}$$

provided the variational void radiation conductivity $\lambda_r^*(\mu)$ is identified to be

$$\lambda_r^*(\mu)(Cb)^{-1} = \chi_0 - 2\mu\chi_0 + \mu^2(\chi_0 + \lambda_0) - (\chi_1 - \mu\chi_1 - \mu\lambda_1)^2(\chi_2 + \lambda_2)^{-1}. \tag{46}$$

For the other parameter ω, at arbitrarily fixed μ, the optimum can be written in terms of P_{opt} from Eqs. 32 and 45 as

$$\mu\omega_{\text{opt}} = \frac{\chi_1 - \mu\chi_1 - \mu\lambda_1}{\chi_2 + \lambda_2}\left(\frac{\lambda_s}{\lambda_r^*(\mu)}\right) \times\left[1 + (F_0 - 2a^{-1}b^{-2})F_0^{-1}P_{\text{opt}}\right]. \tag{47}$$

When the optimized P of Eq. 45 and ω of Eq. 47 are substituted back into the righthand side of inequalities 36a–36i, and the expression Eq. 46 is identified as λ_r^*, the variational expression

$$\frac{\lambda_e}{\lambda_s} \le 1 - \phi + \phi\frac{(2a^{-1}b^{-2} + F_0)\lambda_r^* - F_0\lambda_s}{(2a^{-1}b^{-2} - F_0)\lambda_s + F_0\lambda_r^*}, \tag{48}$$

gives the exact value of λ_e for the corresponding prolate spheroid inclusion in the two-phase conduction model with conductivities λ_r^* and λ_s. With the assignment of λ_r^* in Eq. 46, μ can be explicitly eliminated from the variational effective conductivity, and only an implicit dependence of the variational bound on μ through $\lambda_r^*(\mu)$ remains. Also the λ_e increases monotonically with λ_r^*, hence for the engineering void radiation model conductivity λ_r,

$$\lambda_r \le \lambda_r^*(\mu) \tag{49}$$

for any parameter value of μ,

$$\mu_{\text{opt}} = \left\{\chi_0 - \chi_1(\chi_1 + \lambda_1)(\chi_2 + \lambda_2)^{-1}\right\} \times\left\{\chi_0 + \lambda_0 - (\chi_1 + \lambda_1)^2(\chi_2 + \lambda_2)^{-1}\right\}^{-1}, \tag{50}$$

and the optimum variational void radiation conductivity down the symmetry axis of a prolate spheroidal cavity is

$$\frac{\lambda_r^*}{Cb} = \frac{\chi_0\lambda_0(\chi_2 + \lambda_2) - \chi_0\lambda_1^2 - \chi_1^2\lambda_0}{(\chi_0 + \lambda_0)(\chi_2 + \lambda_2) - (\chi_1 + \lambda_1)^2}. \tag{51}$$

Plots of $\lambda_r^*(Cb)^{-1}$ vs. the cavity surface emissivity and the square of the eccentricity are given in Figures 3a and 3b.

Discussion and Conclusion

The $\lambda_r^*(Cb)^{-1}$ expression, Eq. 51, with χ's and λ's specified, respectively, by Eqs. 39a–41b and 42a–44b, provides from Eq. 48 a best estimate of λ_e, as well as a variational upper bound. In the sense of the model it is an optimized upper bound, Eqs. 49–51, on the void radiation conductivity value. The χ_0, χ_1, and χ_2 functions in Eq. 51, all of which have been evaluated analytically are given, respectively, by Eqs. 39b, 40b, and 41b. Each χ has the form of the emissivity factor $\epsilon(1-\epsilon)^{-1}$, times either a function of the eccentricity α, or a constant. The λ_0, λ_1, and λ_2 terms in Eq. 51 depend only on the cavity shape through α; the first λ_0 is given by

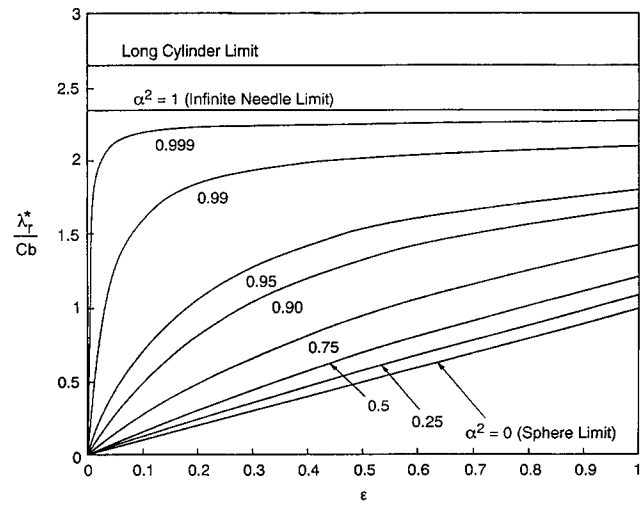

Figure 3a. Dimensionless radiation thermal conductivity vs. surface emissivity for several prolate spheroid squared eccentricities.

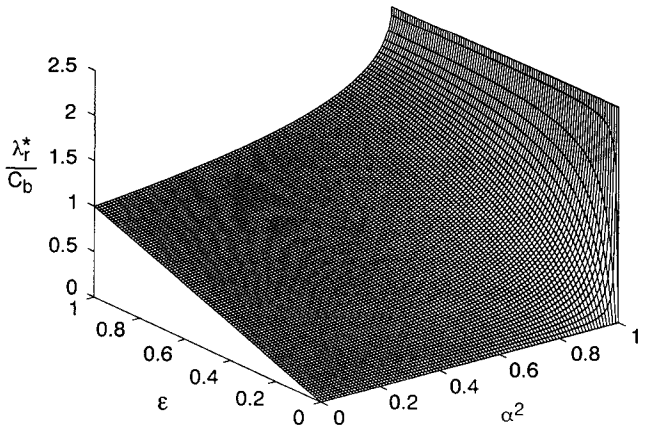

Figure 3b. Corresponding surface in three dimensions.

the analytical equation, Eq. 42c. The other two integrals, λ_1 and λ_2, are evaluated by three-point Newton–Cotes quadrature methods (Ralston and Rabinowitz, 1965). Once λ_1 and λ_2 are done for the elongated spheroid cavity eccentricity range from 0 to 1, the dimensionless void radiation conductivity model is specified for all ϵ and α^2. In Figure 3a, $\lambda_r^*(Cb)^{-1}$ is plotted vs. the surface emissivity for various degrees of elongation from the spherical cavity ($\alpha^2 \to 0$) to a long-needle void ($\alpha^2 \to 1$). Figure 3a also lists the long-cylinder value for comparison. The surface, Figure 3b, demonstrates the nature of the overall behavior of $\lambda_r^*(Cb)^{-1}$ and the four possible limits, $\alpha^2 \to 0$, $\alpha^2 \to 1$, $\epsilon \to 0$, and $\epsilon \to 1$.

Along the lefthand edge of the $\lambda_r^*(Cb)^{-1}$ surface of Figure 3b, the sphere limit $\alpha^2 \to 0$, the dimensionless radiation conductivity increases linearly from zero at $\epsilon = 0$ up to unity at $\epsilon = 1$. In this limit the trial function forms, Eqs. 31 and 33, for T^* and B^* are known to be exact results (Tsai and Strieder, 1985). The opposite limit $\alpha^2 \to 1$ of a long-needle cavity can be seen at the righthand edge of the $\lambda_r^*(Cb)^{-1}$ surface in Figure 3b. The dimensionless radiation conductivity is a constant $3\pi/4$ independent of the surface emissivity for positive ϵ, but drops discontinuously to zero at the point $\epsilon = 0$. As discussed in the article text directly after Eq. 34, the trial functions, Eqs. 31a–34, λ_r^* and λ_e from Eq. 48 are also exact solutions in the $\alpha^2 \to 1$ limit

$$\lim_{\substack{\text{prolate spheroid}\\ \text{long needle}}} \lambda_r(Cb)^{-1} = \begin{cases} 3\pi/4 & 0 < \epsilon \le 1 \quad (52a) \\ 0 & \epsilon = 0. \quad (52b) \end{cases}$$

The needle result is related to radiation down the axis of a very long right-circular cylindrical cavity of radius b and length $2a$ (Tsai and Strieder, 1986)

$$\lim_{\text{cylinder}} \lambda_r(Cb)^{-1} = \begin{cases} 8/3 & 0 < \epsilon \le 1 \quad (53a) \\ 0 & \epsilon = 0, \quad (53b) \end{cases}$$

also shown in Figure 3a. The needle-cavity conductivity down the prolate spheroid central axis for positive ϵ lies below the corresponding cylindrical cavity by a factor of 0.88. For the limiting case, $a \gg b$, the prolate spheroid may be represented by a stack of right-circular cylinders with a common axis of symmetry and elliptically increasing, then decreasing local radii. Since any elemental cylinder in the stack can be a number of radii in length, the cylindrical conductivity (Eq. 53) can be applied with a local radius instead of b, and the volume average of these local cylindrical conductivities over the prolate spheroid gives Eq. 52. Thus, the needle case of elongation is a perfect insulator at either end, with increasing local cross-sectional conductivity to a maximum of Eq. 53 at the center. The λ_r solution and Figure 3 exhibit the significant difference in radiation heat transfer with cavity elongation from the emissivity-dependent spherical cavity to a cylinder-like emissivity independence for the long needle.

The ϵ dependence of $\lambda_r^*(Cb)^{-1}$ in Eq. 51 is entirely contained in χ_0, χ_1, and χ_2, each with a factor $\epsilon(1-\epsilon)^{-1}$. For a black cavity surface ($\epsilon \to 1$), the χ's approach infinity as $\epsilon(1-\epsilon)^{-1}$, and

$$\lim_{\epsilon \to 1} \lambda_r^*(Cb)^{-1} = \lambda_0 = 3(\arcsin \alpha - \alpha\sqrt{1-\alpha^2})(2\alpha^3)^{-1}. \quad (54)$$

The α dependence of λ_0 is from Eq. 42c, and is seen at the back edge of the surface in Figure 3b. The dimensionless variational radiation conductivity, Eq. 54, varies (Figure 3b) with a flat nearly constant emissivity slope from unity at $\alpha^2 = 0$ up to about 1.5 at $\alpha^2 = 0.8$. Then the conductivity experiences a rapid increase with α^2 to the maximum value of $3\pi/4$ at $\alpha^2 = 1$. There appears to be a significant difference in the rate that the cavity radiation conductivity changes with elongation in the neighborhood of the two limiting cases. Also from the radiation conductivity surface of Figure 3b, these effects persist for any fixed ϵ all the way down to lower emissivity values.

In the neighborhood of the perfectly reflecting surface ($\epsilon \to 0$), the behavior of the radiation void conductivity is much different. The χ's become very small and the conductivity $\lambda_r^*(Cb)^{-1}$ of Eq. 51 vanishes for all α^2 values. χ_0 is the leading first-order term in ϵ and

$$\lim_{\epsilon \to 0} \frac{\lambda_r^*}{\chi_0 Cb} = 1. \quad (55)$$

Equation 55 predicts that $\lambda_r^*(Cb)^{-1}$ increases from zero for any α^2, with an ϵ slope $\chi_0(1-\epsilon)/\epsilon$ given by Eqs. 39a or 39b. This slope increases monotonically with α^2 from unity for a spherical cavity with no elongation ($\alpha^2 = 0$), until it diverges as $3\pi[16(1-\alpha^2)]^{-1}$ in the long-needle elongation limit ($\alpha^2 = 1$). These phenomena are evidenced by the front edge of the cavity radiation conductivity curve, Figure 3b, and suggests a discontinuity at the point $\alpha^2 = 1$ and $\epsilon = 0$. We note, that since the simple quadratic variational principle (Eq. 18) is second order in the error from Eqs. 21 and 24, and since the size of the error near the limit depends directly on the distance from the limit, the slopes in the neighborhood of exact limits at the edges $\alpha^2 = 0$, $\alpha^2 = 1$, and $\epsilon = 0$ of Figure 3b, should also be accurate.

On the spherical cavity side, that is, eccentricity values from $\alpha^2 = 0$ up to $\alpha^2 = 0.5$, the variation of $\lambda_r^*(Cb)^{-1}$ in Figure 3a with emissivity is nearly linear. However, increasing elongation above $\alpha^2 = 0.5$ causes a knee to form at a lower emis-

sivity value $\tilde{\epsilon}(\alpha^2)$ that depends on α^2. For emissivities above the knee ($\epsilon > \tilde{\epsilon}$), the void radiation becomes insensitive to ϵ, while below the knee ($\tilde{\epsilon} > \epsilon$) increase in void radiation down the elongated cavity with ϵ is very rapid. As $\alpha^2 \to 1$, the knee moves back to $\epsilon = 0$ and $\lambda_r^*(Cb)^{-1}$ becomes constant at $3\pi/4$ for $\epsilon > 0$ with a step increase from zero at $\epsilon = 0$.

In summary, the article contains the following results.

1. A method to determine the effective conductivity λ_e of a high-temperature solid with void cavity inclusions was presented. The method is based on rigorous surface and volume energy balances, and a variational principle that provides arbitrarily close bounds on λ_e, the quality of engineering interest. The engineering-model concept of a solid and void radiation conductivity is used to formulate the trial functions. One consequence is that the results can be readily cast in terms of current engineering models that use radiation conductivities in process calculations. A void radiation conductivity λ_r^* is obtained (Eq. 51), which can be interpreted either as an upper bound and estimate of λ_r, or at least a means to obtain the best value of the effective conductivity λ_e.

2. The dimensionless coefficient $\lambda_r^*(Cb)^{-1}$ of radiant heat transfer down the symmetry axis of a prolate spheroid of arbitrary eccentricity α and surface emissivity ϵ is obtained (Figures 3a and 3b). Exact solutions are developed in the neighborhood of low emissivity $\epsilon \to 0$ for any α^2, the neighborhood of no elongation, that is, the sphere limit $\alpha^2 \to 0$ for any ϵ, and the region of maximum elongation to a long needle $\alpha^2 \to 1$ for any ϵ. For nonvanishing emissivities, the $\lambda_r^*(Cb)^{-1}$ surface (Figure 3b) exhibits several interesting characteristics with elongation. The dimensionless radiation conductivity varies from a linearly increasing function of the emissivity for a sphere ($\alpha^2 = 0$) to a substantially higher, emissivity independent value for a long needle ($\alpha^2 = 1$). In the region of modest elongation $0 \le \alpha^2 < 0.5$ and for any fixed nonvanishing ϵ the $\lambda_r^*(Cb)^{-1}$ surface is rather flat and not very steep in the α^2 direction, but above $\alpha^2 = 0.8$ the radiation conductivity increases rapidly with elongation.

The model also exhibits quite different behavior at low emissivities. While the cavity radiation conductivity always vanishes at zero emissivity for any α^2, the ϵ slope in this region, while unity for no elongation, becomes singular as the cavity is stretched. For α^2 above 0.5, a knee develops in the emissivity curve below which $\lambda_r^*(Cb)^{-1}$ increases rapidly with emissivity and above which it is asymptotic.

3. Usable expressions (Eqs. 51, 56, and 57) for λ_r^* down an elongated spheroidal cavity are obtained in terms of χ and λ functions (Eqs. 39–44).

The formulation of a reciprocal, variational lower bound (Strieder and Aris, 1973) on the effective conductivity will require certain mathematical conditions on the trial functions. In the solid phase, the trial temperature for the reciprocal variational principle must have a vanishing Laplacian, which is the case for the trial form, Eqs. 31a and 31b, used here. But in addition to obtaining a rigorous variational lower bound, the trial radiosity must satisfy an integral equation of the same type as Eq. 8. At the present time, an analytical solution of this equation is not known, even for the simplest one-dimensional geometries, and as a result the reciprocal variational principle calculation cannot be done. An example of this type of problem in variational analysis can be found in Strieder and Prager (1967).

Notation

d^3r = differential volume located at $\boldsymbol{r}$ in the solid, V_s
F = ellipsoidal perturbation function defined in Eq. 31b
$I(\boldsymbol{r})$ = linearized form of the black-body emission flux from Eq. 15
$\boldsymbol{j}$ = Cartesian directional unit vector shown in Figure 1
$\boldsymbol{j}'$ = rotated Cartesian position unit vector for $\boldsymbol{r}'$ shown in Figure 1
$\boldsymbol{k}$ = Cartesian directional vector shown in Figure 1
L = solid slab thickness
m = average pore radius
Q = net heat flux across plane of the slab in the x-direction per unit surface area
$\boldsymbol{r}$ = location vector pointing from the prolate spheroid center
x, x = Cartesian coordinate reactor and magnitude running from $-L/2$ to $L/2$ across the slab length
$\boldsymbol{y}, y$ = Cartesian coordinate vector and magnitude
$\boldsymbol{y}', y'$ = rotated Cartesian coordinate position vector and magnitude for the point $\boldsymbol{r}'$ shown in Figure 1
z, z = Cartesian coordinate vector and magnitude
η_x = x-component of the surface normal vector $\boldsymbol{\eta}$
$\boldsymbol{\theta}, \theta$ = solid temperature gradient vector and its magnitude in Eq. 17
ϕ = cavity volume fraction

Literature Cited

Argo, W. B., and J. M. Smith, "Heat Transfer in Packed Beds," *Chem. Eng. Progr.*, **49**, 443 (1953).

Beek, J., "Design of Packed Bed Reactors," *Adv. Chem. Eng.*, **3**, 203 (1962).

Berman, A. S., "Free Molecule Transmission Properties," *J. Appl. Phys.*, **36**, 3356 (1965).

Chiew, Y. C., and E. D. Glandt, "Simultaneous Conduction and Radiation in Porous Composite Materials: Effective Thermal Conductivity," *Ind. Eng. Chem. Fundam.*, **22**, 276 (1983).

Devera, A., and W. Strieder, "Upper and Lower Bounds on the Thermal Conductivity of a Random, Two-Phase Medium," *J. Phys. Chem.*, **81**, 1783 (1977).

Ganguley, B. K., and D. P. H. Hasselman, "Effect of Matrix Conductivity on the Radiation Heat Transfer Across Spherical Pores," *J. Amer. Ceram. Soc.*, **59**, 83 (1976).

Kaganer, M. G., *Thermal Insulation in Cryogenic Engineering*, IPST Press, Jerusalem (1969).

Landau, L. D., E. M. Lifshitz, and L. P. Pitaevskiĭ, *Electrodynamics of Continuous Media*, 2nd ed., Pergamon Press, New York (1984).

Marino, G. P., "Radiation Transfer Across a Spherical Pore in a Linear Temperature Gradient," *Trans. Metall. Soc. AIME*, **245**, 821 (1969).

Marino, G. P., "The Porosity Correction Factor for the Thermal Conductivity of Ceramic Fuels," *J. Nucl. Mater.*, **38**, 178 (1971).

Ralston, A., and P. Rabinowitz, *A First Course in Numerical Analysis*, McGraw-Hill, New York (1978).

Siegel, R., and J. R. Howell, *Thermal Radiation Heat Transfer*, 3rd ed., McGraw-Hill, New York (1992).

Smith, J. M., *Chemical Engineering Kinetics*, 2nd ed., McGraw-Hill, New York (1970).

Smith, J. M., *Chemical Engineering Kinetics*, 3rd ed., McGraw-Hill, New York (1981).

Sortirchos, S. V., and M. M. Tomadakis, "Modeling Transport Reaction and Pore Structure Evolution during Densification of Cellular or Fibrous Structures," *Mat. Res. Soc. Sym. Proc.*, **108**, 73 (1990).

Strieder, W., and R. Aris, *Variational Methods Applied to Problems of Diffusion and Reaction*, Springer-Verlag, Berlin (1973).

Strieder, W., and S. Prager, "Upper and Lower Bounds on Knudsen Flow Rates," *J. Math. Phys.*, **3**, 514 (1967).

Torquato, S., "Thermal Conductivity of Disordered Heterogeneous Media from the Microstructure," *Rev. Chem. Eng.*, **4**, 151 (1987).

Tsai, D. S., and W. Strieder, "Radiation Across a Spherical Cavity Having both Specular and Diffuse Reflectance Components," *Chem. Eng. Sci.*, **41**, 170 (1985).

Tsai, D. S., and W. Strieder, "Specular and Diffuse Reflections in Radiant Heat Transport Across and Down a Cylindrical Pore," *Ind. Eng. Chem. Fundam.*, **25**, 244 (1986).

Varma, A., G. Cao, and M. Morbidelli, "Self-Propagating Solid-Solid Noncatalytic Reactions in Finite Pellets," *AIChE J.*, **36**, 1039 (1990).
Verhoff, F. H., and W. Strieder, "Numerical Studies of Knudsen Diffusion and Chemical Reaction in Capillaries of Finite Length," *Chem. Eng. Sci.*, **26**, 245 (1971).
Whitaker, S., "Radiant Energy Transport in Porous Media," *Ind. Eng. Chem. Fundam.*, **19**, 210 (1980).
Whitaker, S., "Moisture Transport Mechanisms During the Drying of Granular Porous Media," *Proc. Int. Drying Symp.*, Vol. 1, Kyoto, Japan, p. 31 (1984).

Appendix A: χ Functions for a Prolate Spheroid

We define the integral $\Lambda_{i,j}$ over the cavity surface Σ of the ellipsoid shown in Figure 1

$$\Lambda_{i,j} = \langle (\boldsymbol{i}\cdot\boldsymbol{r}/b)^i (\boldsymbol{i}\cdot\boldsymbol{\eta})^j \rangle_\Sigma, \qquad (i,j=0,1,2) \qquad \text{(A1)}$$

in terms of the surface average (Eq. 35b), or directly as

$$\Lambda_{i,j} = \Sigma^{-1} \int_\Sigma d^2\boldsymbol{r} (\boldsymbol{i}\cdot\boldsymbol{r}/b)^i (\boldsymbol{i}\cdot\boldsymbol{\eta})^j, \qquad \text{(A2)}$$

and note that $\chi_0 = \epsilon(1-\epsilon)^{-1}(2b/m)\Lambda_{2,0}$; $\chi_1 = \epsilon(1-\epsilon)^{-1}(2b/m)\Lambda_{1,1}$; $\chi_2 = \epsilon(1-\epsilon)^{-1}(2b/m)\Lambda_{0,2}$; and $\Lambda_{0,0} = 1$.

As the prolate ellipsoid is a surface and volume of revolution

$$\Lambda_{i,j} = 2\pi\Sigma^{-1} \int_{-a}^{a} y\,dx \left[\frac{ds}{dx}\right] \left(\frac{x}{b}\right)^i \eta_x^j, \qquad \text{(A3)}$$

where ds is the arc length element on the ellipse ($x^2a^{-2} + y^2b^{-2} = 1$) that corresponds to dx. From the geometry (Figure 1) of the ellipse ds/dx and η_x can be recast in terms of x and the $\Lambda_{i,j}$ become the one-dimensional integrals

$$\Lambda_{i,j} = 2\pi\Sigma^{-1} \int_{-a}^{a} dx[(1-\alpha^2)^{1/2}(a^2-\alpha^2x^2)^{1/2}] \times \left(\frac{x}{b}\right)^i [-x(1-\alpha^2)^{1/2}(a^2-\alpha^2x^2)^{-1/2}]^j, \qquad \text{(A4)}$$

which can be readily evaluated for the i,j choices of interest. The final integrated forms are

$$\Lambda_{0,0} = 1 = \Sigma^{-1} 2\pi b^2 \left\{1 + (\alpha\sqrt{1-\alpha^2})^{-1} \arcsin\alpha\right\}, \qquad \text{(A5)}$$

which assigns the cavity surface area Σ,

$$\Lambda_{2,0} = \Sigma^{-1}\pi b^2 [2(1-\alpha^2)\alpha^2]^{-1} \times \left\{2\alpha^2 - 1 + (\alpha\sqrt{1-\alpha^2})^{-1} \arcsin\alpha\right\}, \qquad \text{(A6)}$$

$$\Lambda_{1,1} = -\Sigma^{-1}\frac{4}{3}\pi b^2 (\sqrt{1-\alpha^2})^{-1}, \qquad \text{(A7)}$$

and

$$\Lambda_{0,2} = -\Sigma^{-1} 2\pi b^2 (1-\alpha^2)\alpha^{-2} \left\{1 - (\alpha\sqrt{1-\alpha^2})^{-1} \arcsin\alpha\right\}. \qquad \text{(A8)}$$

Appendix B: One-Dimensional Kernel Down the Symmetry Axis of a Prolate Spheroid

If Σ_{dx} is the cavity surface isolated when planes x and $x + dx$ are cut across the cavity cross section perpendicular to the x-axis in Figure 1, the one-dimensional kernel is defined to be

$$K(x,x')\,dx\,dx' = \int_{\Sigma_{dx}} d^2\boldsymbol{r} \int_{\Sigma_{dx'}} d^2\boldsymbol{r}'\, K(\boldsymbol{r},\boldsymbol{r}'), \qquad \text{(B1)}$$

or in terms of the arc lengths ds and ds', along the ellipse, that corresponds, respectively, to dx and dx'

$$K(x,x') = \int_0^{2\pi} \frac{ds}{dx} y\,d\psi \int_0^{2\pi} \frac{ds'}{dx'} y'\,d\psi'\, K(\boldsymbol{r},\boldsymbol{r}'), \qquad \text{(B2)}$$

where ψ and ψ' are the angles of rotation relative to the symmetry axis as shown in Figure 1. The displacement vector $\boldsymbol{\rho}$ from $\boldsymbol{r}$ to $\boldsymbol{r}'$

$$\boldsymbol{\rho} = (x'-x)\boldsymbol{i} + y'\boldsymbol{j}' - y\boldsymbol{j}, \qquad \text{(B3)}$$

the unit normals in the form

$$\boldsymbol{\eta} = (\boldsymbol{i}\cdot\boldsymbol{\eta})\boldsymbol{i} + (\boldsymbol{j}\cdot\boldsymbol{\eta})\boldsymbol{j} \qquad \text{(B4)}$$

and $K(\boldsymbol{r},\boldsymbol{r}')$ from Eq. 5, when substituted into Eq. B2, give

$$K(x,x') = -\pi^{-1} \int_0^{2\pi} \frac{ds}{dx} y\,d\psi \int_0^{2\pi} \frac{ds'}{dx'} y'\,d\psi' \times [(x'-x)\boldsymbol{i}\cdot\boldsymbol{\eta} + (-y + y'\cos\psi)\boldsymbol{j}\cdot\boldsymbol{\eta}] \times [(x'-x)\boldsymbol{i}\cdot\boldsymbol{\eta}' + (y' - y\cos\psi)\boldsymbol{j}'\cdot\boldsymbol{\eta}'] \times [(x'-x)^2 + (y')^2 + y^2 - 2yy'\cos\psi]^{-2}. \qquad \text{(B5)}$$

The ψ angular dependence of the integrand in Eq. B5 is explicit, all other functions depend only on x or x' and can be obtained from the geometry of the ellipse. We then have the one-dimensional K for a prolate spheroid

$$\frac{K(x,x')}{\pi} = 1 - |x'-x|\alpha^2\{\alpha^4[2a^2 + x^2 + 4xx' + (x')^2] - \alpha^2[10a^2 + 6xx'] + 8a^2\} \times \{\alpha^4(x'+x)^2 - 4\alpha^2xx' + 4a^2(1-\alpha^2)\}^{-3/2} \qquad \text{(B6)}$$

and note that in the limits $\alpha^2 \to 0$ the one-dimensional kernels for a sphere (Tsai and Strieder, 1986), and $\alpha^2 \to 1$ the one-dimensional kernel for a cylinder (Verhoff and Strieder, 1971) are obtained.

Manuscript received Mar. 20, 1996, and revision received June 12, 1996.